Abstract submitted to the AHS International 73rd Annual Forum & Technology Display
To be held at Fort Worth, TX, May 9-11, 2017

(Technical Session: Aerodynamics)

Navier-Stokes Simulation of UH-60A Rotor/Wake Interaction Using Adaptive Mesh Refinement

Neal M. Chaderjian†
NASA Ames Research Center, Moffett Field, CA, 94035

Nomenclature

c_{tip}	blade-tip chord	R	rotor radius
C_T	rotor thrust coefficient	Re_{tip}	Reynolds number at blade tip
M_∞	free-stream Mach number	α_s	rotor shaft angle
M_{tip}	blade-tip Mach number	β	rotor side-slip angle
M^2C_n	blade sectional normal force coefficient times local Mach number squared	ΔS	Cartesian wake-grid spacing
		Δt	physical time step
M^2C_m	blade sectional pitching moment coefficient times local Mach number squared	μ	advance ratio
		σ	rotor solidity
r	radial distance from hub center	ψ	azimuth angle

Introduction

NASA's Revolutionary Vertical Lift Technology (RVLT) project is working towards increasing a helicopter's forward-flight speed and performance in an environmentally responsible manner, e.g., to reduce noise levels and fuel consumption. However, these new designs can lead to a helicopter's blade-tip vortices remaining in the path of other rotor blades, causing blade vortex interaction (BVI) and dynamic stall. The airloads can be challenging to accurately predict for these flow conditions, even with high-fidelity computational fluid dynamics (CFD). Dynamic stall in particular has been the subject of decades of experimental and computational study, especially in two dimensions. Dynamic stall is characterized by the formation of the blade's leading edge vortex, it's detachment and downwind advection past the blade's trailing edge, and a negative pitching moment.

Recent CFD studies[1] have demonstrated that the prediction accuracy of rotor blade airloads and performance for hover and high-speed forward flight do not require high-resolution vortex wakes, as previously thought. Typical rotor wake grid spacing for engineering analysis is $\Delta S=10\%c_{tip}$. High-resolution wake grids can be 2-4 times finer in each spatial direction, resulting in grids systems that are more than an order-of-magnitude larger than engineering simulations, and too costly for routine analysis. However these examples have vortex wakes that descend below the rotor blades, thus avoiding significant blade/wake interaction. Two examples are shown in Fig. 1 for a UH-60A rotor in hover and forward flight. The forward flight conditions described in this paper are summarized in Table 1.

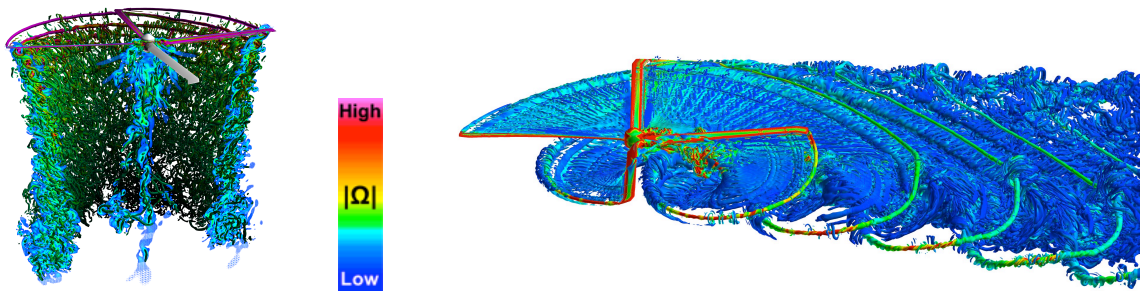

a) Hover ($C_T/\sigma=0.102$), $\Delta S=5\%\ c_{tip}$,. b) Forward flight (Counter C8534), $\Delta S=2.5\%\ c_{tip}$.

Figure 1 UH-60A rotor wakes colored by vorticity magnitude.

† Senior Research Scientist, M/S 258-2, Neal.Chaderjian@nasa.gov, Member AHS.

Table 1 UH60-A flight counter flow conditions.

Flight Counter	M_∞	M_{Tip}	μ	Re_{tip}	α_s, deg	β, deg	C_T
C8534 (High Speed)	0.236	0.642	0.368	6.86×10^6	-7.31	1.28	0.00651
C8513 (BVI)	0.0982	0.643	0.153	7.15×10^6	0.75	7.71	0.00657
C9017 (Dynamic Stall)	0.158	0.666	0.237	4.62×10^6	-0.15	-1.58	0.0110

This paper addresses two important questions: 1) To what degree does the CFD quantitative accuracy depend on resolving the flow features with finer grids, as apposed to the inherent limitations of the turbulence model; 2) Does the two-dimensional (2D) dynamic stall analog adequately represent the problem in three dimensions (3D)? Adaptive mesh refinement (AMR) in the rotor wake is used to address part of the first question for the BVI and dynamic stall cases listed in Table 1. Using near-body AMR on the blade surfaces will be the subject of another study. CFD flow visualization will provide some fundamental insight into the nature and cause of 3D dynamic stall.

Numerical Approach

The Overflow 2.2L CFD code[2] has been used to simulate a 4-bladed UH60-A rotor with a simplified hub for the BVI and dynamic stall flow conditions listed in Table 1. The rotor geometry and overset curvilinear body grids are shown in Fig. 2. Examples of the Cartesian off-body (OB) AMR wake grids on a center-body plane are shown in Figs. 3 and 6. Each rotor blade has 121,423 surface grid points and 10.7 million volume grid points. Each rotor blade consists of four O-grids (two main blade grids, and two inboard/outboard blade-tip cap grids). The main blade O-grid is split into two overlapping overset grids to facilitate future NB AMR simulations on the rotor blades. The total grid points for the BVI and dynamic stall cases in this paper range in size from 78 million – 1.8 billion grid points, depending on the rotor-wake OB AMR grid resolution. Unless otherwise noted, AMR will hereafter refer to Cartesian OB AMR.

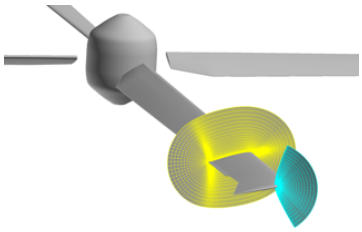

Figure 2. UH60-A rotor blade grids and hub geometry.

All cases solve the time-dependent Navier-Stokes equations throughout the entire computational domain, where the blade grids rotate through a background AMR grid system. The present simulations use 5th-order low diffusion central differencing for the convective terms (7-point difference stencil) and artificial dissipation. Second order accurate dual-time stepping is used, where the physical time step Δt=¼ degrees of rotation, and 60 sub-iterations ensures convergence to the new time level. The Spalart-Allmaras DDES turbulence model[3] is applied to all grids. Further details of the numerical approach and accuracy can be found in Ref. 1. Blade flexibility and trimmed blade-motions are modeled by loosely coupling OVERFLOW with the CAMRAD II helicopter comprehensive analysis code.[4] The converged loosely-coupled approach provides aeroelastic blade deflections for trimmed steady flight.[1]

Numerical Results

Two forward flight conditions are now briefly presented. Only a small subset of the available results and analysis are shown in this abstract due to page-limit restrictions. All CFD solutions and analysis are complete, and will be included in the final paper.

Flight Counter C8513 (BVI):

The BVI case was computed with three AMR wake-grid resolutions of ΔS=10% c_{tip}, ΔS=5% c_{tip}, and ΔS=2.5% c_{tip}. Each case consisted of 81 million, 293 million, and 1.8 billion grid points, respectively. Figure 3 shows the AMR process finding and refining the vortex wake on the rotor center-body plane, and an oblique view of the vortex wake visualized by an iso-surface of the q-criterion. Notice that there are three vortices riding on top of the forward-most rotor blade, which will generate noise.

The azimuthal variation of the computed normal force coefficient (minus the mean) is compared with experiment in Fig. 4 at four radial locations along the rotor blade, and for all three AMR resolutions. The outboard peaks located at $\psi \approx 90^\circ$ and 270° are the result of BVI. Overall, the comparison is quite good, and all three AMR resolutions are giving almost identical results.

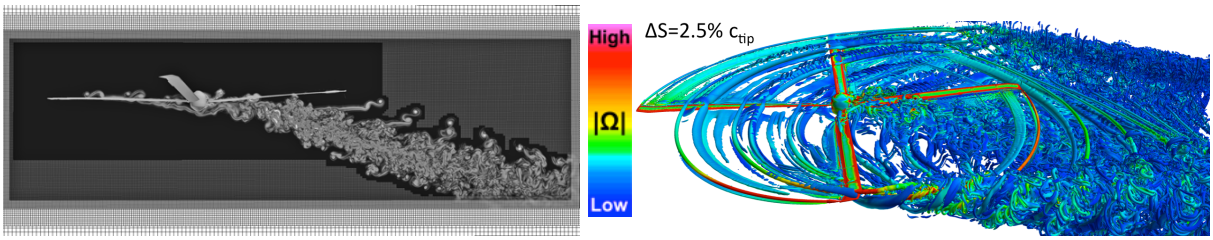

Figure 3 Rotor center-body plane AMR and oblique view of vortex wake.

The computed pitching moment coefficient (mean removed) is compared with experiment in Fig. 5. The comparison is very good, similar to the results in Fig. 4, and once again all three AMR resolutions are virtually identical. The two outboard BVI events at $\psi \approx 90^\circ$ and 270° are again evident. The BVI moment peak near $\psi \approx 270^\circ$ is somewhat under predicted at r/R=0.865, but improved at r/R=0.965, where the surface mesh is finer. Near-body AMR may improve the prediction of pitching moment amplitude for the outboard radial locations.

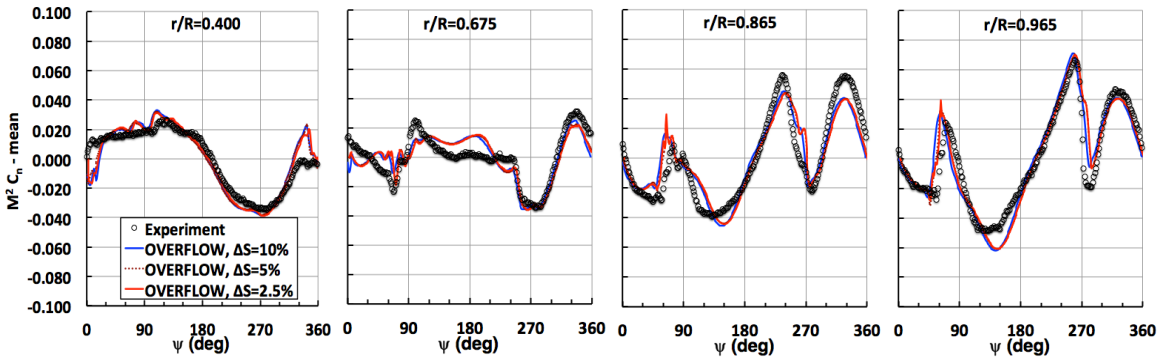

Figure 4 Comparison of normal force coefficient (mean removed) at four radial stations.

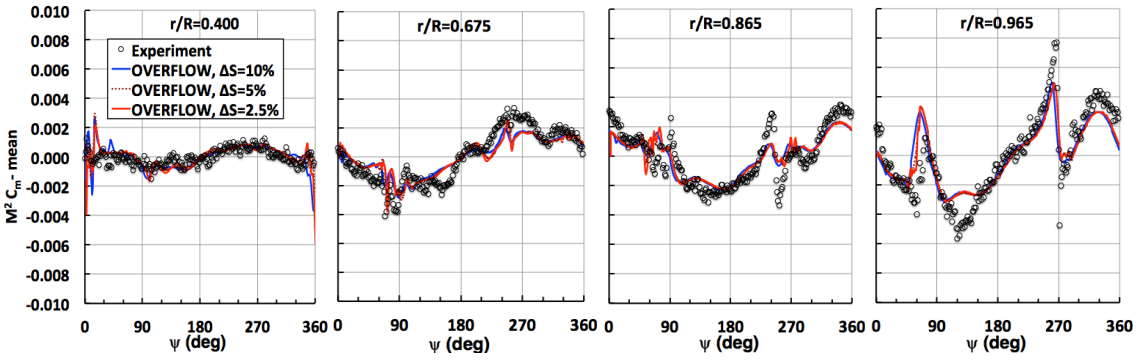

Figure 5 Comparison of pitching moment coefficient (mean removed) at four radial stations.

Flight Counter C9017 (Dynamic Stall):

The dynamic stall case was similarly computed with three AMR wake-grid resolutions of ΔS=10% c_{tip}, ΔS=5% c_{tip}, and ΔS=2.5% c_{tip}. Each case consisted of 78 million, 236 million, and 1.3 billion grid points, respectively. Figure 6 shows the AMR process finding and refining the vortex wake on the rotor center-body plane, and an oblique view of the vortex wake visualized by an iso-surface of the q-criterion. Notice that there are two vortices riding on top of the forward-most rotor blade, which will generate noise and play an important role in the dynamic stall process. Flow separation begins in the third quadrant and advects downwind into the 4th quadrant.

Figure 7 compares the computed normal force coefficient (mean removed) with experiment at four radial locations. The agreement between computation and experiment is good, however, the drop in normal force is under predicted near $\psi \approx 90^{\circ}$ for the outboard sections.

The predicted pitching moment coefficient shown in Fig. 8 is in good overall agreement with the flight-test data. The negative pitching moment in the 4th quadrant is captured well at r/R=0.865, but is larger (negatively) at r/R=0.675 and 0.965. The 4th quadrant is particularly challenging due to the strong interaction of the rotor blade with the turbulent wake created by the dynamic stall event and hub.

It is noted that the accuracy of the airloads prediction for this dynamic stall case does not significantly depend on the resolution of the wake grid, similar to the previous BVI case. Moreover, the CFD airloads validation presented in this paper are similar to the results reported by Ahmad and Biedron[5] for flight counters C8513 and C9017. They used the unstructured FUN3D and structured OVERFLOW CFD codes with a ΔS=10% c_{tip} wake grid resolution, similar to the coarsest wake grid resolution presented in this paper.

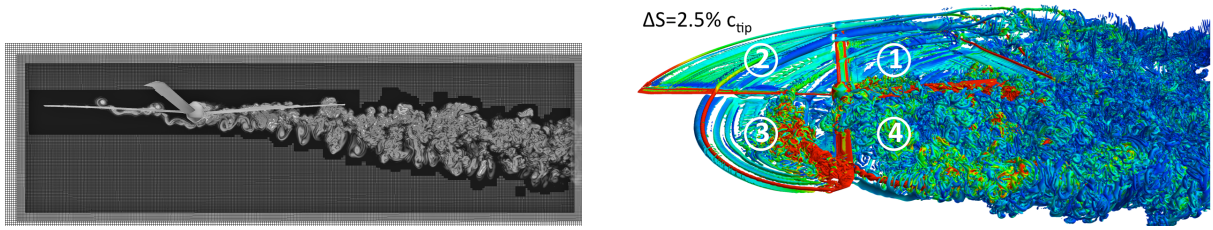

Figure 6 Rotor center-body plane AMR and oblique view of vortex wake showing quadrants 1-4.

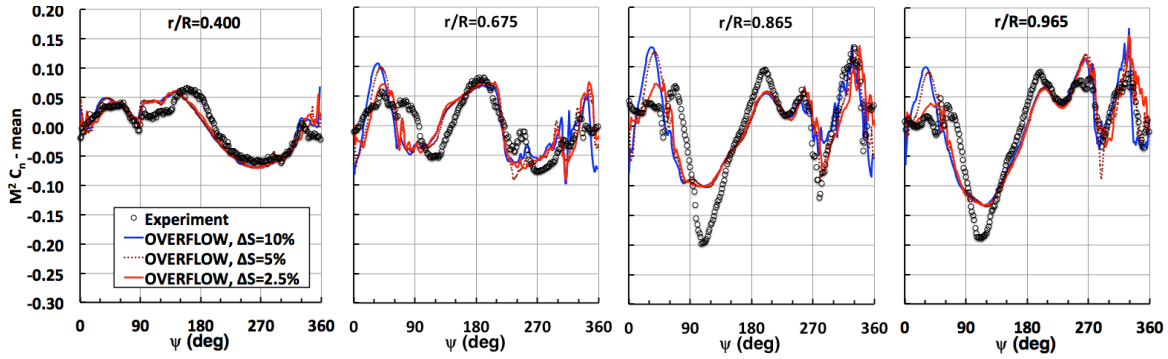

Figure 7 Comparison of normal force coefficient (mean removed) at four radial stations.

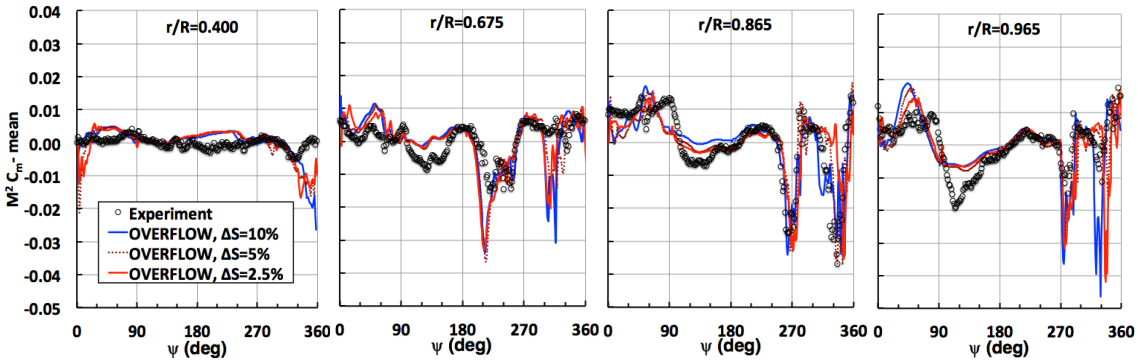

Figure 8 Comparison of pitching moment coefficient (mean removed) at four radial stations.

Figure 9 shows the development of dynamic stall for Blade 3. The two frames in the figure are separated by an azimuth angle of $\Delta\psi = 45^{\circ}$. The first frame shows the vortex of Blade 4 passing over Blade 3 with no flow separation. The second frame (45 degrees later) shows outboard flow separation on Blade 3, which is caused by the

Blade 4 vortex. The spin of the vortex decreases the local angle of attack just inboard of the vortex to about 4 degrees, resulting in attached flow. The spin of the vortex also increases the local angle of attack just outboard of the vortex to about 19 degrees, resulting in flow separation. Due to the influence of the vortex, separation is limited to a small spanwise width. As Blade 3 rotates, the vortex and its separation move radially outboard together towards the blade tip. A similar process occurs on the inboard part of Blade 3 from Blade 1's tip vortex (2 blades upwind in rotation). As Blade 3 rotates, the inboard vortex and its separation move towards the hub. Thus Blade 3 experiences separation on its inboard and outboard radial locations, and attached flow in-between. In this 3D example, dynamic stall occurs due to the presence of blade-tip vortices passing over a rotor blade rather than the 2D perspective of pure pitch oscillation of the local airfoil section. Additional details will be presented in the final paper.

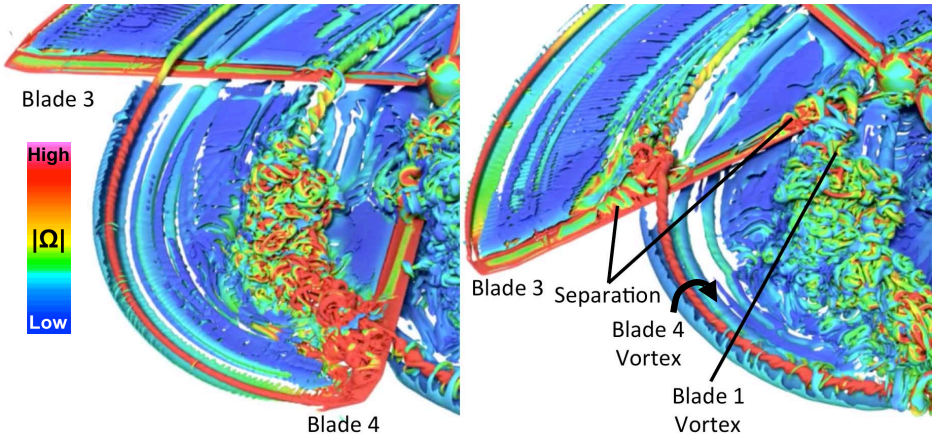

Figure 9 Close-up view of blades three and four, $\Delta\psi_{\text{Blade 3}} = 45^{\circ}$, ΔS=2.5% c_{tip}.

Summary and Final Paper

High-resolution simulations of rotor/vortex-wake interaction for a UH60-A rotor under BVI and dynamic stall conditions were carried out with the OVERFLOW Navier-Stokes code.

- The normal force and pitching moment variation with azimuth angle were in good overall agreement with flight-test data, similar to other CFD results reported in the literature.
- The wake-grid resolution did not have a significant effect on the rotor-blade airloads. This surprising result indicates that a wake grid spacing of ΔS=10% c_{tip} is sufficient for engineering airloads prediction for hover and forward flight. This assumes high-resolution body grids, high-order spatial accuracy, and a hybrid RANS/DDES turbulence model.
- Three-dimensional dynamic stall was found to occur due the presence of blade-tip vortices passing over a rotor blade on the retreating side. This changed the local airfoil angle of attack, causing stall, unlike the 2D perspective of pure pitch oscillation of the local airfoil section.

The final paper will include a complete description of the flow simulations, including more detailed validation with experiment, and a more detailed analysis of the physical mechanisms leading to 3D dynamic stall.

References

[1]Chaderjian, N. M., "Advances in Rotor Performance and Turbulent Wake Simulation using DES and Adaptive Mesh Refinement," Paper Number ICCFD7-3506, Presented at the 7th International Conference on Computational Fluid Dynamics on the Big Island of Hawaii, July 9-13, 2012.

[2]Buning, P. G., Jespersen, D. C., Pulliam, T. H., Chan, W. M., Slotnick, J. P., Krist, S. E., and Renze, K. J., "Overflow User's Manual" NASA Langley Research Center, Hampton, VA, 2002.

[3]Spalart, P. R., Deck, S., Sur, M. L., Squires, K. D., Strelets, M. and Travin, A., "A New Version of Detached-Eddy Simulation, Resistant to Ambiguous Grid Densities," *Theoretical and Computational Fluid Dynamics (2006)*, Vol. 20, No. 3, pp. 181-195.

[4]Johnson, W., "Rotorcraft Aerodynamic Models for a Comprehensive Analysis," American Helicopter Society 54th Annual Forum, Washington, D.C., May 1998.

[5]Ahmad, J.U., and Biedron, R.T., "Code-to-Code Comparison of CFD/CSD Simulation for a Helicopter Rotor in Forward Flight," AIAA 2011-3819, June 2011.